LETTER

https://doi.org/10.1038/s41586-018-0618-9

In-plane anisotropic and ultra-low-loss polaritons in a natural van der Waals crystal

Weiliang Ma[1,11], Pablo Alonso-González[2,11]*, Shaojuan Li[1,11], Alexey Y. Nikitin[3,4], Jian Yuan[1], Javier Martín-Sánchez[2], Javier Taboada-Gutiérrez[2], Iban Amenabar[5], Peining Li[5], Saül Vélez[5,6], Christopher Tollan[5], Zhigao Dai[7], Yupeng Zhang[7], Sharath Sriram[8], Kourosh Kalantar-Zadeh[9], Shuit-Tong Lee[1], Rainer Hillenbrand[4,5,10]* & Qiaoliang Bao[1,7]*

Polaritons—hybrid light–matter excitations—enable nanoscale control of light. Particularly large polariton field confinement and long lifetimes can be found in graphene and materials consisting of two-dimensional layers bound by weak van der Waals forces[1,2] (vdW materials). These polaritons can be tuned by electric fields[3,4] or by material thickness[5], leading to applications including nanolasers[6], tunable infrared and terahertz detectors[7], and molecular sensors[8]. Polaritons with anisotropic propagation along the surface of vdW materials have been predicted, caused by in-plane anisotropic structural and electronic properties[9]. In such materials, elliptic and hyperbolic in-plane polariton dispersion can be expected (for example, plasmon polaritons in black phosphorus[9]), the latter leading to an enhanced density of optical states and ray-like directional propagation along the surface. However, observation of anisotropic polariton propagation in natural materials has so far remained elusive. Here we report anisotropic polariton propagation along the surface of α-MoO_3, a natural vdW material. By infrared nano-imaging and nano-spectroscopy of semiconducting α-MoO_3 flakes and disks, we visualize and verify phonon polaritons with elliptic and hyperbolic in-plane dispersion, and with wavelengths (up to 60 times smaller than the corresponding photon wavelengths) comparable to those of graphene plasmon polaritons and boron nitride phonon polaritons[3–5]. From signal oscillations in real-space images we measure polariton amplitude lifetimes of 8 picoseconds, which is more than ten times larger than that of graphene plasmon polaritons at room temperature[10]. They are also a factor of about four larger than the best values so far reported for phonon polaritons in isotopically engineered boron nitride[11] and for graphene plasmon polaritons at low temperatures[12]. In-plane anisotropic and ultra-low-loss polaritons in vdW materials could enable directional and strong light–matter interactions, nanoscale directional energy transfer and integrated flat optics in applications ranging from biosensing to quantum nanophotonics.

Anisotropic optical materials exhibit numerous distinctive and non-intuitive optical phenomena such as negative refraction[13], hyper-lensing[14], wave-guiding[15] and enhanced quantum radiation[16], which have been demonstrated typically with artificial hyperbolic metamaterials. However, further progress is limited by optical losses and the complexity of metamaterial fabrication[17].

The recent emergence of low-loss vdW materials opens the door to achieving anisotropic optical phenomena naturally, because their layered crystal structure leads to an intrinsic and strong out-of-plane (perpendicular to the layers) optical anisotropy[5,18]. Prominent examples are hyperbolic phonon polaritons (PhPs)—infrared light coupled to lattice vibrations in layered polar materials—in hexagonal boron nitride (h-BN), which exhibit long lifetimes[11], ultra-slow propagation[19] and hyper-lensing effects[20,21]. Interestingly, when the layers of a vdW material are anisotropic (that is, when the permittivities along orthogonal in-plane directions are different), the polaritons are expected to propagate along the layers with an in-plane anisotropic dispersion[9]. When the permittivities are different but of the same sign, the polaritons possess an elliptic in-plane dispersion, in which the iso-frequency contours (slices in two-dimensional (2D) wavevector space (k_x, k_y) of constant frequency ω) describe ellipsoids. When the signs are different, the polaritons possess an in-plane hyperbolic dispersion, in which the iso-frequency contours are open hyberboloids[22]. Only recently, PhPs with in-plane hyperbolic dispersion have been demonstrated by fabricating an artificial metamaterial out of h-BN flakes[23].

Theory predicts polaritons with both in-plane anisotropies even for natural materials (without any nanostructuring) that exhibit an in-plane anisotropy of their electronic or structural properties: for example, hyperbolic plasmons—light coupled to free carriers—in black phosphorus[9] or in Weyl semimetals[24]. While being expected to provide fundamental insights into exotic material properties (for example, non-reciprocal Purcell enhancement[24]), they also bear application potential, including intrinsically non-reciprocal plasmon guiding[25], topological transitions in 2D anisotropic plasmons[22] and directional nanoscale energy collimation[26] (for use as planar and directional light emitters with on-chip integration). However, their experimental observation and verification has so far been elusive. Here we present the first (to our knowledge) images of in-plane elliptic and hyperbolic polaritons (more precisely, PhPs) that propagate with record-length lifetimes. We found them in thin slabs of α-phase molybdenum trioxide (α-MoO_3), a natural vdW polar semiconductor. Phonon polaritons have been observed[27] only recently in α-MoO_3, but their anisotropic propagation properties have not been described.

The diagrams in Fig. 1a, b show the orthorhombic crystal structure of α-MoO_3, in which layers formed by distorted MoO_6 octahedra (Fig. 1a) are weakly bound by vdW forces[28] and all three lattice constants (*a*, *b* and *c*) are different (Fig. 1b). Most importantly, α-MoO_3 has strong in-plane structural anisotropy, caused by the interlayer spacing of the (100) facet differing from that of the (001) facet by as much as 7.2%, which leads to the highly anisotropic response[29] (Supplementary Information). Indeed, the different directional vibrations of the α-MoO_3 crystal structure yield two infrared 'reststrahlen bands' (RBs)[30] between about 820 cm^{-1} and 1,010 cm^{-1}; in this range, the typically strong reflectivity between the transverse optical and longitudinal optical phonon frequencies (TOs and LOs, respectively) shows a large in-plane anisotropy (Supplementary Information). Thus, we can expect that in-plane anisotropic PhPs exist in this material. An optical microscopy image of the α-MoO_3 flakes and their typical Raman spectrum

---

[1] Institute of Functional Nano and Soft Materials (FUNSOM), Jiangsu Key Laboratory for Carbon-based Functional Materials and Devices, and Collaborative Innovation Center of Suzhou Nano Science and Technology, Soochow University, Suzhou, China. [2] Departamento de Física, Universidad de Oviedo, Oviedo, Spain. [3] Donostia International Physics Center (DIPC), Donostia-San Sebastián, Spain. [4] IKERBASQUE, Basque Foundation for Science, Bilbao, Spain. [5] CIC nanoGUNE, Donostia-San Sebastián, Spain. [6] Department of Materials, ETH Zürich, Zürich, Switzerland. [7] Department of Materials Science and Engineering, and ARC Centre of Excellence in Future Low-Energy Electronics Technologies (FLEET), Monash University, Clayton, Victoria, Australia. [8] Functional Materials and Microsystems Research Group and MicroNano Research Facility, RMIT University, Melbourne, Australia. [9] School of Chemical Engineering, University of New South Wales (UNSW), Kensington, New South Wales, Australia. [10] CIC nanoGUNE and UPV/EHU, Donostia-San Sebastián, Spain. [11] These authors contributed equally: W. Ma, P. Alonso-González, S. Li. *e-mail: pabloalonso@uniovi.es; r.hillenbrand@nanogune.eu; qiaoliang.bao@monash.edu

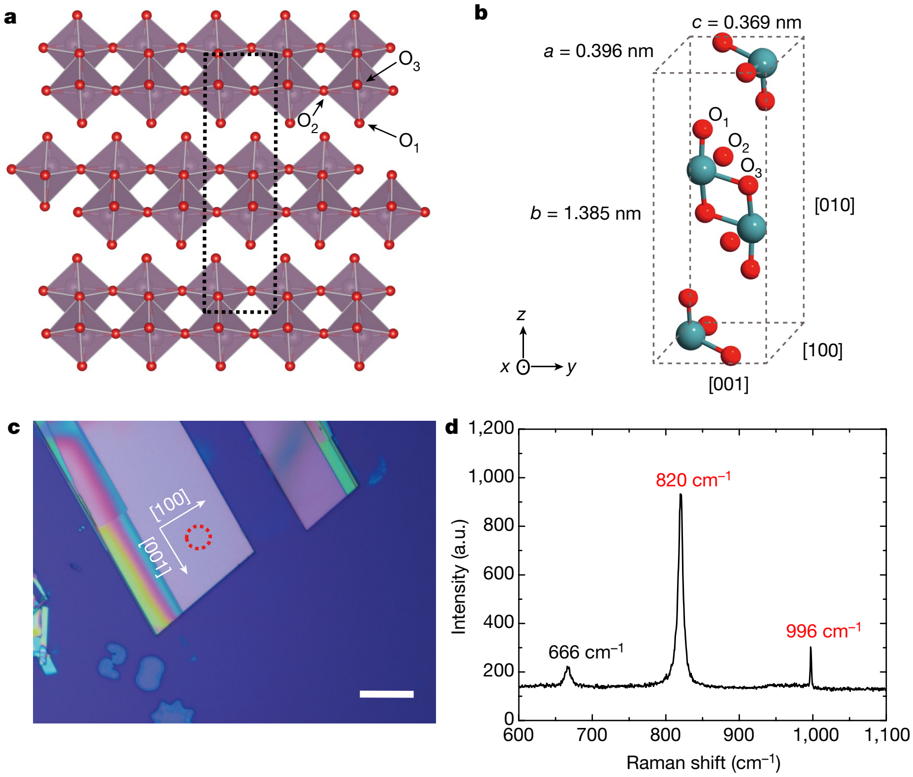

Fig. 1 | Physical properties of α-MoO_3. **a**, Illustration of the orthorhombic lattice structure of layered α-MoO_3 (red spheres, oxygen atoms). The orthorhombic structure is based on bilayers of distorted MoO_6 octahedra stacked along the [010] direction via vdW interactions. The three possible positions of oxygen atoms are denoted O_{1-3}, and the unit cell is shown dashed. **b**, Schematic of the unit cell of α-MoO_3; the lattice constants are $a = 0.396$ nm, $b = 1.385$ nm and $c = 0.369$ nm. Blue spheres, molybdenum atoms. **c**, Optical image of α-MoO_3 flakes. The α-MoO_3 crystals typically appear to be rectangular owing to the anisotropic crystal structure. Labelled arrows indicate crystal directions. Scale bar, 20 μm. **d**, Raman spectrum taken in the area marked by a red dashed circle in **c**. Red frequency labels indicate the Raman peaks associated with the lattice vibrations producing the RBs of α-MoO_3.

are shown in Fig. 1c, d, respectively. The latter shows[30] characteristic peaks at 820 cm^{-1} and 996 cm^{-1} associated with the lattice vibrations producing the RBs of α-MoO_3.

To explore the polaritonic response of α-MoO_3, we performed polariton interferometry using scattering-type scanning near-field optical microscopy (s-SNOM, Fig. 2a). A vertically oscillating metallized atomic force microscopy (AFM) tip is illuminated with p-polarized infrared light of frequency ω and field E_{inc} while scanning an α-MoO_3 flake. Acting as an infrared antenna[3–5], the tip concentrates the incident field at its very apex to give a nanoscale infrared spot for local probing of material properties and for exciting polaritons. The tip-scattered radiation is recorded simultaneously with topography, yielding nanoscale resolved near-field images (Methods). Specifically, the polaritons (described by the field E and wavelength λ) excited by the tip propagate away and are back-reflected at the flake edges, giving rise to interference fringes with a spacing $\lambda/2$.

Figure 2b shows s-SNOM near-field amplitude images of an α-MoO_3 flake with thickness $d = 250$ nm taken at $\omega = 990$ cm^{-1} and $\omega = 900$ cm^{-1}, both frequencies residing[30] inside the two RBs of α-MoO_3. For $\omega = 990$ cm^{-1} (top image) we observe bright fringes parallel to all the flake edges. They strongly resemble PhPs, similar to what has been observed in s-SNOM experiments on other polar materials[5] and recently on[27] α-MoO_3. We observe that the fringe periodicity largely depends on the propagation direction, being $\lambda_x = 950$ nm and $\lambda_y = 1{,}200$ nm for the [100] and [001] crystal directions (Supplementary Information), respectively. Apart from the deep subwavelength-scale polariton confinement $\lambda_{x,y} \ll \lambda_0 = 11.1$ μm (where λ_0 is the wavelength of the illuminating infrared light), this finding reveals a strongly anisotropic in-plane propagation (along the flake). This anisotropy becomes even more marked at $\omega = 900$ cm^{-1} (Fig. 2b lower image), where the fringes are seen only parallel to the [001] direction.

For unambiguous verification of the anisotropic polariton propagation, we recorded spectroscopic line scans[5] (Methods) along the [100] and [001] in-plane crystal directions (Fig. 2d, left and right panels, respectively). We observe two spectral bands exhibiting a series of signal maxima (fringes). The band limits (indicated by the horizontal dashed lines) correspond to the LO and TO phonon frequencies of α-MoO_3 (denoted by LO_1, LO_2, TO_1 and TO_2) and thus reveal the upper and lower RBs (U-RB and L-RB, respectively). In the U-RB we find that the fringe spacing (corresponding to the polariton wavelength) along both the [100] and [001] directions increases with increasing frequency, indicating a negative phase velocity (analogous to PhPs in the lower type-I RB of h-BN[19]). As in Fig. 2b, we observe a slightly different fringe spacing for the [100] and [001] directions, but now for all frequencies between TO_2 and LO_2. A very different behaviour is observed for the L-RB. Along the [100] direction we see fringes whose spacing decreases with increasing frequency, manifesting polaritons with positive phase velocity. More importantly, along the [001] direction we do not observe signal oscillations at a fixed frequency for the whole spectral range between TO_1 and LO_1. This finding indicates the absence of PhPs propagating in the [001] direction, supporting our assumption of a hyperbolic in-plane dispersion. The horizontal fringes observed in Fig. 2d (right panel) are caused by polaritons propagating along the [100] direction. Note that a line profile for a fixed ω corresponds to a vertical line profile (along the [001] direction, and thus parallel to the interference fringes) in the lower panel of Fig. 2b, where we can see that PhPs are launched by the left edge of the flake. Depending on ω and on the distance between the tip and the left flake edge, we thus observe either a constantly bright or dark contrast when the tip is scanned along the [001] direction, corresponding to a bright or dark horizontal fringe in the right panel of Fig. 2d.

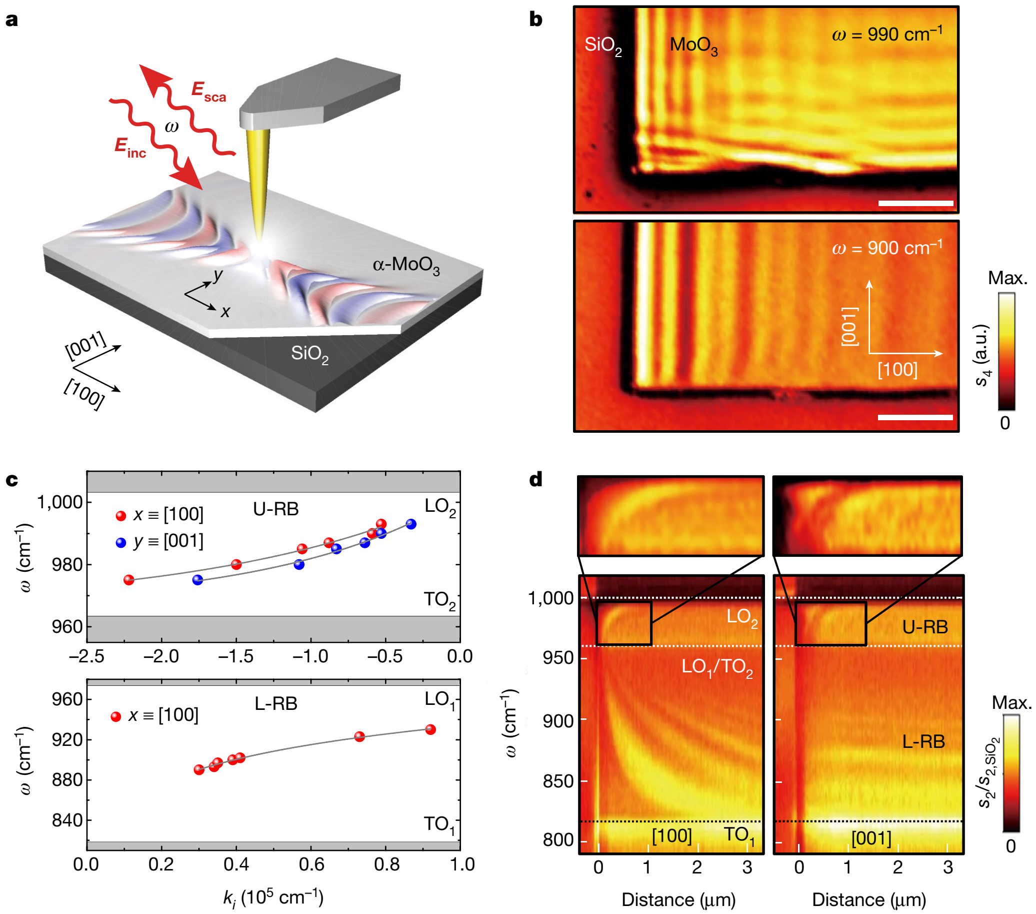

Fig. 2 | Real-space imaging and nano-spectroscopy of an α-MoO$_3$ flake. **a**, Schematic of the s-SNOM experimental configuration used to image an α-MoO$_3$ flake. A metallized AFM tip (yellow) is illuminated by p-polarized infrared light of frequency ω and electric field E_{inc}. It launches polaritons, which are back-reflected at the flake edges and subsequently scattered by the tip. The tip-scattered field E_{sca} is detected by a distant detector. **b**, Near-field amplitude images s_4 (Methods) of an α-MoO$_3$ flake with thickness $d = 250$ nm at illuminating frequencies $\omega = 990$ cm^{-1} (top panel) and $\omega = 900$ cm^{-1} (bottom panel). Scale bars, 2 μm. **c**, Dispersion of PhPs along the [100] and [001] directions in the U-RB (top panel) and L-RB (bottom panel, see text). Grey lines in both panels are guides to the eye. Grey shaded areas indicate the spectral regions outside the RBs. **d**, Bottom row, nano-FTIR spectral line scans along [100] and [001] (directions shown as arrows in the bottom panel of **b**), showing the near-field amplitude s_2 (normalized to the near-field amplitude on the SiO$_2$ substrate, s_{2,SiO_2}) as a function of distance between tip and flake edge. Dotted lines mark the approximate longitudinal and transversal phonon modes in α-MoO$_3$ (TO$_1$, 820 cm^{-1}; LO$_1$/TO$_2$, 963 cm^{-1}; LO$_2$, 1,003 cm^{-1}). Top row, zooms into the boxed areas of the U-RB shown in the bottom row.

For a better understanding and quantitative analysis of the anisotropic polariton propagation, we extracted the PhP dispersions, $\omega(k_i)$ ($i = x, y$), from monochromatic s-SNOM images (not shown) of the flake in Fig. 2b. The dispersions for both crystal directions and RBs are plotted in Fig. 2c. For the U-RB (upper panel), the PhP dispersions along both crystal directions are similar, although slightly separated from each other (that is, for the same frequency ω, we measured different wavevectors k_i). This result verifies that PhPs in the U-RB propagate with in-plane anisotropy. By plotting the complex-valued wavevector of the PhPs, we find that their phase velocity, $v_{p,i} = \omega/k_i$, is negative along both directions, which is indicated by negative k_i values. Furthermore, the remarkably small slopes of the dispersion curves (Supplementary Information) yield unprecedentedly small group velocities ($v_{g,i} = (\partial k_i/\partial\omega)^{-1}$) of about $0.8 \times 10^{-3}c$ (at $\omega = 985$ cm^{-1}), which in the future could be exploited for strong light–matter interaction experiments[31]. For the L-RB (Fig. 2c lower panel), we only display the dispersion of the PhPs for the [100] direction, as no PhPs are observed in the orthogonal [001] direction. In this case, the phase velocity is positive (indicated by positive k_x values), and the group velocity is about $0.7 \times 10^{-2}c$ (at $\omega = 893$ cm^{-1}), which is comparable to that of ultra-slow PhPs in h-BN[11].

To quantify the anisotropy of the PhPs and to measure their iso-frequency contours in wavevector space, we analyse PhP propagation along all possible directions on the flake. To that end, we fabricated disks of α-MoO$_3$ (Methods) and performed polariton interferometry experiments (Supplementary Information) analogous to those reported in Fig. 2. Figure 3a, b shows typical near-field amplitude images taken at frequencies respectively in the U-RB ($\omega = 983$ cm^{-1}) and in the L-RB ($\omega = 893$ cm^{-1}) of α-MoO$_3$. In the U-RB, the interference pattern shows an elliptical shape with the largest PhP wavelength along the [001] surface direction, which continuously reduces to its smallest value along the orthogonal [100] surface direction. More strikingly, in the L-RB the interference pattern manifests as an almond shape, in which the PhPs have their largest wavelength along the [100] direction and which continuously reduces to zero until no discernible polariton propagation occurs along the orthogonal [001] direction. By Fourier transform of Fig. 3a, b, we obtain the iso-frequency contours directly. We find an ellipsoid in the U-RB (Fig. 3c) and a hyperbola in the L-RB (Fig. 3d), revealing that the PhPs exhibit elliptic and hyperbolic dispersions, respectively. Note that Fig. 3c shows two ellipses instead of one, differing by a factor of 2 in their semi-axes. We attribute this observation to the presence of both tip- and edge-launched PhPs[32,33] in Fig. 3a (Supplementary Information). On the other hand, the hyperbola in Fig. 3d opens along the [001] direction, which indicates that PhPs along this crystal direction are forbidden, thus explaining the observations in Figs. 2, 3b.

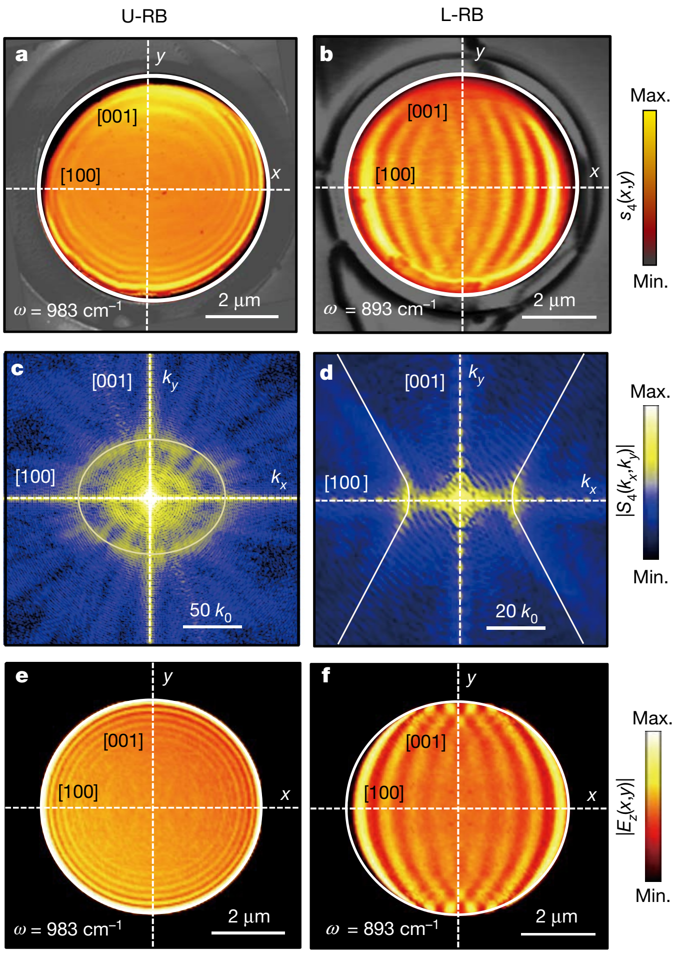

Fig. 3 | In-plane elliptical and hyperbolic PhPs in an α-MoO$_3$ disk. **a**, **b**, Near-field amplitude images s_4 of an α-MoO$_3$ disk (colour key at right) with $d = 144$ nm. The imaging frequencies are $\omega = 983$ cm^{-1} (U-RB; **a**), and 893 cm^{-1} (L-RB; **b**). Dashed white lines indicate the [100] and [001] surface directions. Scale bars, 2 μm. **c**, **d**, Absolute value of the Fourier transform $|S_4(k_x,k_y)|$ of the near-field images in **a** and **b**, respectively (colour key at right), revealing the iso-frequency contours for each RB. Solid lines show the iso-frequency contours of the PhPs obtained by fitting equation (1) for each case (note that they correspond to $2k$). Scale bars are $50k_0$ and $20k_0$, for the U-RB and L-RB respectively, with k_0 being the momentum of light in free space. **e**, **f**, Calculated near-field amplitude images $|E_z(x,y)|$ (Supplementary Information) for an α-MoO$_3$ disk (colour key at right) at $\omega = 983$ cm^{-1} (U-RB; **e**) and 893 cm^{-1} (L-RB; **f**). Scale bars, 2 μm.

To corroborate our experimental results theoretically, and to extract the as-yet unknown anisotropic permittivity of α-MoO$_3$, we model the α-MoO$_3$ flake as a 2D conductivity layer of zero thickness (Methods). We find the following dispersion relation for polaritons in a thin in-plane anisotropic slab surrounded by two dielectric half-spaces with isotropic permittivities ε_1 and ε_2 (Supplementary Information):

$$\left[k_x^2\alpha_{xx}+k_y^2\alpha_{yy}+\frac{k_0k_t^2}{2}\left(\frac{\varepsilon_1}{k_{z1}}+\frac{\varepsilon_2}{k_{z2}}\right)\right]\left[k_y^2\alpha_{xx}+k_x^2\alpha_{yy}+\frac{k_t^2}{2k_0}(k_{z1}+k_{z2})\right] \\ -k_x^2k_y^2(\alpha_{xx}-\alpha_{yy})^2=0 \tag{1}$$

where $k_{x,y}$ and $k_{z1,2}=\sqrt{\varepsilon_{1,2}k_0^2-k_x^2-k_y^2}$ are the in- and out-of-plane wavevectors, respectively, $k_0 = 2\pi/\lambda_0$ is the wavevector in free space, and $\hat{\alpha} = 2\pi\hat{\sigma}_{\mathrm{eff}}/c$ is the normalized conductivity, introduced for convenience. Using equation (1) with α_{xx} and α_{yy} as fitting parameters, we obtain excellent agreement with the elliptical and hyperbolic features in Fig. 3c, d, where our fits are shown as white solid lines. Neglecting absorption, we find $\alpha_{xx} = -0.12i$ ($\varepsilon_{xx} = 2.6$) and $\alpha_{yy} = -0.16i$ ($\varepsilon_{yy} = 3.7$) for $\omega = 983$ cm^{-1} (U-RB), and $\alpha_{xx} = 0.26i$ ($\varepsilon_{xx} = -6.4$) and $\alpha_{yy} = -0.07i$ ($\varepsilon_{yy} = 1.7$) for $\omega = 893$ cm^{-1} (L-RB).

We corroborate the model and permittivity values by numerical simulation of near-field images of an α-MoO$_3$ disk on SiO$_2$ (Supplementary Information). We used the nominal experimental values of 144 nm and 6 μm for the disk thickness and diameter, respectively, and the anisotropic real-valued permittivities obtained from the fit described above. The imaginary parts of the permittivities and the value of ε_{zz} (not obtained from the fit) were adjusted to obtain the best matching of the experimental images and of the sign of the phase velocities in each RB. As a result of our analysis, we find $\varepsilon_{xx} > 0$, $\varepsilon_{yy} > 0$ and $\varepsilon_{zz} < 0$ for the elliptic U-RB, and $\varepsilon_{xx} < 0$, $\varepsilon_{yy} > 0$ and $\varepsilon_{zz} > 0$ for the hyperbolic L-RB (Supplementary Information). The simulated polariton interferometry amplitude images are shown in Fig. 3e, f. Their excellent agreement with the experiments (Fig. 3a, b) validates both the model and the permittivity values. The results demonstrate that experimental PhP interferometry of α-MoO$_3$ disks and fitting of the results with our simple theoretical model allow the highly anisotropic local permittivities of α-MoO$_3$ to be extracted.

The conductivity tensor $\hat{\sigma}_{\mathrm{eff}}$—and thus the wavevectors of the PhPs—depends on the slab thickness d. According to the relation between $\hat{\sigma}_{\mathrm{eff}}$ and $\hat{\varepsilon}$ (see Methods), we obtain from equation (1) the thickness-dependent anisotropic in-plane polariton wavevectors (Supplementary Information):

$$k_i \approx -\frac{\varepsilon_1+\varepsilon_2}{d\varepsilon_{ii}}, i=x,y \tag{2}$$

In Fig. 4a, we demonstrate the thickness tunability of in-plane hyperbolic polaritons: we plot the PhP dispersions obtained by s-SNOM nano-imaging along the [100] crystal direction of α-MoO$_3$ flakes with different thickness d. We clearly observe that the wavevector k_x and thus the polariton confinement increase with decreasing thickness. For $d = 55$ nm, we find k_x values of about 3.5×10^5 cm^{-1}, corresponding to a PhP wavelength of 180 nm. This value is 60 times smaller than $\lambda_0 = 10.8$ μm, suggesting that in-plane anisotropic propagation could be well paired with deep subwavelength-scale field confinement for the development of ultra-compact devices. The inverse dependence of k_x on d is better observed in Fig. 4b, where we plot the experimental k_x (red dots) obtained at $\omega = 902$ cm^{-1} for four flakes of different thickness. These experimental values are well matched by our equation (2) (grey curve), where we used $\varepsilon_{xx} = -5.1$ as extracted for the flake with $d = 144$ nm in Fig. 3, thus strongly supporting the validity of our approximation.

A key property of polaritons for future applications is their lifetime[10,11]. To measure it, we fitted s-SNOM amplitude line profiles along the [100] direction (blue and red crosses in Fig. 4c) with an exponentially decaying sine-wave function corrected by the geometrical spreading factor $\sqrt{x}$ (Supplementary Information)[10]. From the amplitude decay length L_x (one of the fitting parameters) we obtain the lifetime according to $\tau_x = L_x/v_g$, where the group velocity v_g is taken from Fig. 2c. For the in-plane hyperbolic PhPs we obtain $\tau_x = 1.9 \pm 0.3$ ps, which reveals the ultra-low-loss character of these polaritons. Surprisingly, for the in-plane elliptic PhPs we obtain $\tau_x = 8 \pm 1$ ps (four times higher than that of PhPs in isotropically enriched h-BN[11]). On some flakes we find lifetimes up to 22 ps (Supplementary Information). We note that in contrast to low-loss h-BN PhPs[11] and graphene plasmons[12], a rather small number of fringes were observed on α-MoO$_3$ flakes. This can be explained by the small group velocities of the MoO$_3$ PhPs, which yield relatively short propagation lengths. The ultra-long PhP lifetimes are corroborated by the ultra-narrow linewidths of the α-MoO$_3$ Raman peaks (Supplementary Information) at 996 cm^{-1} and 820 cm^{-1} (corresponding to anisotropic bond stretching modes[30] that originate in the U-RB and L-RB, respectively), revealing very high crystal quality. A similar relation has been recently reported to explain the large lifetimes observed in isotopically enriched h-BN[11].

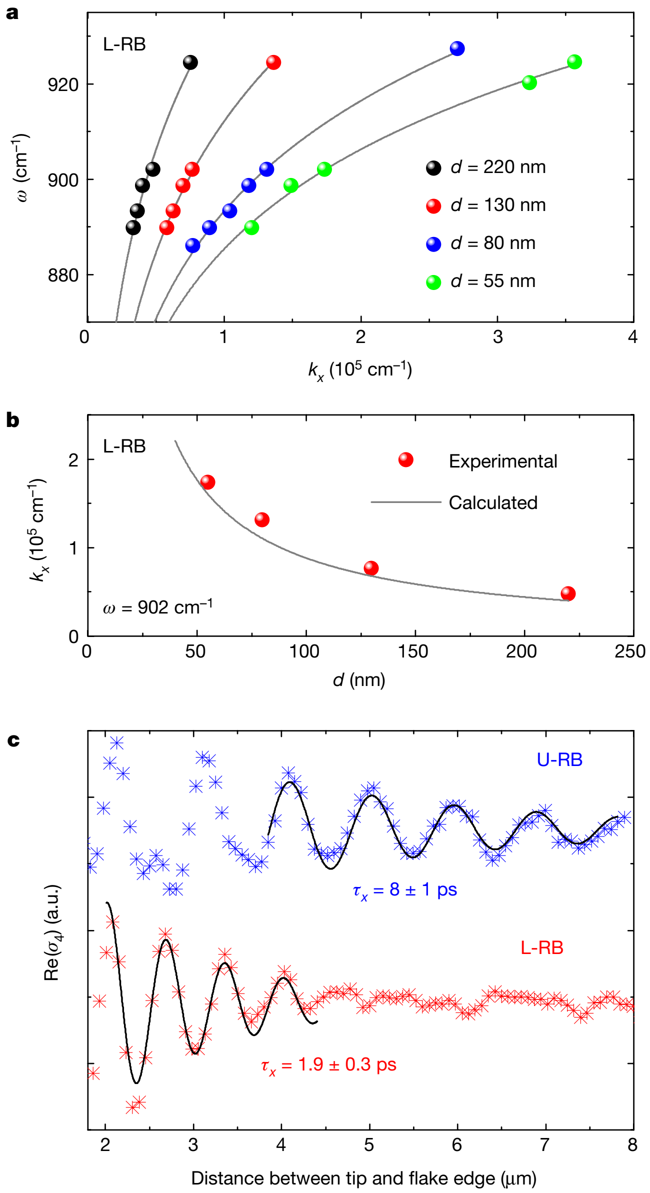

Fig. 4 | Thickness tunability and lifetime of in-plane hyperbolic and elliptic PhPs in α-MoO$_3$. a, Experimental (dots) PhP dispersions along the [100] direction in α-MoO$_3$ for a varying flake thickness d (lines are guides to the eyes). **b**, Experimental (dots) and calculated (line) dependence of k_x upon d. **c**, s-SNOM line traces (showing the real part of the complex-valued s-SNOM signal σ_4; Methods) along the [100] direction of the flake shown in Fig. 2b with $d = 250$ nm in the elliptic (blue crosses, $\omega = 990$ cm^{-1}) and hyperbolic (red crosses, $\omega = 930$ cm^{-1}) regimes. Damped sine-wave functions (black solid lines) were fitted to the data that correspond to edge-launched PhPs (Supplementary Information). Amplitude lifetimes $\tau_x = 8 \pm 1$ ps and $\tau_x = 1.9 \pm 0.3$ ps are obtained for the U-RB and L-RB, respectively.

In-plane anisotropic α-MoO$_3$ PhPs add a new member to the growing list of polaritons in vdW materials. In combination with external stimuli, such as strain, electric gating or photo-injection of carriers, we envisage active tuning of the anisotropic PhP properties. Our findings may thus establish a route to directional control of light and light–matter interactions at the nanoscale.

Online content

Any methods, additional references, Nature Research reporting summaries, source data, statements of data availability and associated accession codes are available at https://doi.org/10.1038/s41586-018-0618-9.

Received: 8 April 2018; Accepted: 17 August 2018;
Published online: 24 October 2018

1. Basov, D., Fogler, M. & de Abajo, F. G. Polaritons in van der Waals materials. *Science* **354**, aag1992 (2016).
2. Low, T. et al. Polaritons in layered two-dimensional materials. *Nat. Mater.* **16**, 182–194 (2017).
3. Fei, Z. et al. Gate-tuning of graphene plasmons revealed by infrared nano-imaging. *Nature* **487**, 82–85 (2012).
4. Chen, J. et al. Optical nano-imaging of gate-tunable graphene plasmons. *Nature* **487**, 77–81 (2012).
5. Dai, S. et al. Tunable phonon polaritons in atomically thin van der Waals crystals of boron nitride. *Science* **343**, 1125–1129 (2014).
6. Chakraborty, S. et al. Gain modulation by graphene plasmons in aperiodic lattice lasers. *Science* **351**, 246 (2016).
7. Cai, X. et al. Plasmon-enhanced terahertz photodetection in graphene. *Nano Lett.* **15**, 4295–4302 (2015).
8. Rodrigo, D. et al. Mid-infrared plasmonic biosensing with graphene. *Science* **349**, 165–168 (2015).
9. Low, T. et al. Plasmons and screening in monolayer and multilayer black phosphorus. *Phys. Rev. Lett.* **113**, 106802 (2014).
10. Woessner, A. et al. Highly confined low-loss plasmons in graphene–boron nitride heterostructures. *Nat. Mater.* **14**, 421–425 (2015).
11. Giles, A. J. et al. Ultralow-loss polaritons in isotopically pure boron nitride. *Nat. Mater.* **17**, 134–139 (2018).
12. Ni, G. X. et al. Fundamental limits to graphene plasmonics. *Nature* **557**, 530–533 (2018).
13. Hoffman, A. J. et al. Negative refraction in semiconductor metamaterials. *Nat. Mater.* **6**, 946–950 (2007).
14. Liu, Z., Lee, H., Xiong, Y., Sun, C. & Zhang, X. Far-field optical hyperlens magnifying sub-diffraction-limited objects. *Science* **315**, 1686 (2007).
15. Podolskiy, V. A. & Narimanov, E. E. Strongly anisotropic waveguide as a nonmagnetic left-handed system. *Phys. Rev. B* **71**, 201101 (2005).
16. Cortes, C. L., Newman, W., Molesky, S. & Jacob, Z. Quantum nanophotonics using hyperbolic metamaterials. *J. Opt.* **14**, 063001 (2012).
17. Takayama, O., Bogdanov, A. A. & Lavrinenko, A. V. Photonic surface waves on metamaterial interfaces. *J. Phys. Condens. Matter* **29**, 463001 (2017).
18. Caldwell, J. D. et al. Sub-diffractional volume-confined polaritons in the natural hyperbolic material hexagonal boron nitride. *Nat. Commun.* **5**, 5221 (2014).
19. Yoxall, E. et al. Direct observation of ultraslow hyperbolic polariton propagation with negative phase velocity. *Nat. Photon.* **9**, 674–678 (2015).
20. Li, P. et al. Hyperbolic phonon-polaritons in boron nitride for near-field optical imaging and focusing. *Nat. Commun.* **6**, 7507 (2015).
21. Dai, S. et al. Subdiffractional focusing and guiding of polaritonic rays in a natural hyperbolic material. *Nat. Commun.* **6**, 6963 (2015).
22. Gomez-Diaz, J. S., Tymchenko, M. & Alù, A. Hyperbolic plasmons and topological transitions over uniaxial metasurfaces. *Phys. Rev. Lett.* **114**, 233901 (2015).
23. Li, P. et al. Infrared hyperbolic metasurface based on nanostructured van der Waals materials. *Science* **359**, 892–896 (2018).
24. Song, J. C. W. & Rudner, M. S. Fermi arc plasmons in Weyl semimetals. *Phys. Rev. B* **96**, 205443 (2017).
25. Mazor, Y. & Steinberg, B. Z. Longitudinal chirality, enhanced nonreciprocity, and nanoscale planar one-way plasmonic guiding. *Phys. Rev. B* **86**, 045120 (2012).
26. Kildishev, A. V., Boltasseva, A. & Shalaev, V. M. Planar photonics with metasurfaces. *Science* **339**, 1232009 (2013).
27. Zheng, Z. et al. Highly confined and tunable hyperbolic phonon polaritons in van der Waals semiconducting transition metal oxides. *Adv. Mater.* **30**, 1705318 (2018).
28. de Castro, I. A. et al. Molybdenum oxides — from fundamentals to functionality. *Adv. Mater.* **29**, 1701619 (2017).
29. Lajaunie, L., Boucher, F., Dessapt, R. & Moreau, P. Strong anisotropic influence of local-field effects on the dielectric response of α-MoO$_3$. *Phys. Rev. B* **88**, 115141 (2013).
30. Py, M. A., Schmid, P. E. & Vallin, J. T. Raman scattering and structural properties of MoO$_3$. *Nuovo Cimento B* **38**, 271–279 (1977).
31. Caldwell, J. D. et al. Low-loss, infrared and terahertz nanophotonics using surface phonon polaritons. *Nanophotonics* **4**, 44–68 (2015).
32. Dai, S. et al. Efficiency of launching highly confined polaritons by infrared light incident on a hyperbolic material. *Nano Lett.* **17**, 5285–5290 (2017).
33. Hu, F. et al. Imaging the localized plasmon resonance modes in graphene nanoribbons. *Nano Lett.* **17**, 5423–5428 (2017).

Acknowledgements We thank S. C. Dhanabalan and J. S. Ponraj for their efforts in the early stages of this project. We thank M. H. Lu, L. Liu, C. W. Qiu and L. Wang for suggestions, and H. Yan and Q. Xing for their assistance with micro-FTIR measurements. We thank Quantum Design China (Beijing laboratory) for technical support of some s-SNOM measurements. This work was performed in part at the Melbourne Centre for Nanofabrication (MCN) in the Victorian Node of the Australian National Fabrication Facility (ANFF). We acknowledge support from the National Natural Science Foundation of China (grant numbers 51222208, 51290273, 51601131, 61604102, 51702219 and 91433107), the Youth 973 programme (2015CB932700), the National Key Research and Development Program (2016YFA0201900), ARC (DP140101501, IH150100006, FT150100450 and CE170100039), the Natural Science Foundation of Jiangsu Province (BK20150053), the Priority Academic Program Development of Jiangsu Higher Education Institutions (PAPD), the Collaborative Innovation Center of Suzhou Nano Science and Technology, and the Spanish Ministry of Economy, Industry and Competitiveness (national projects MAT2015-65525-R, FIS2014-60195-JIN, MAT2017-88358-C3-3-R, MAT2014-53432-C5-4-R, and the project MDM-2016-0618 of the Maria de Maeztu Units of Excellence Programme). Q.B. acknowledges support from the Australian Research Council (ARC) Centre of Excellence in Future Low-Energy Electronics Technologies (FLEET). P.A.-G. acknowledges support from the European Research Council under Starting Grant 715496, 2DNANOPTICA. J.M.-S. acknowledges support through the Clarín Programme from the Government of the Principality of Asturias and a Marie Curie-COFUND grant (PA-18-ACB17-29). P.L. acknowledges support from a Marie Sklodowska-Cuire individual fellowship (SGPCM-705960).

Reviewer information *Nature* thanks A. Chaves and the other anonymous reviewer(s) for their contribution to the peer review of this work.

Author contributions W.M., P.A.-G. and S.L. contributed equally to this work. Q.B. conceived the initial measurements on α-MoO$_3$. R.H., P.A.-G. and Q.B. supervised the project. W.M. and P.A.-G. carried out the near-field imaging experiments with the help of I.A., J.M.-S., J.T.-G., Z.D. and P.L. J.Y. carried out the far-field experiments. W.M., P.A.-G., A.Y.N., S.L., R.H. and Q.B. participated in data analysis and co-wrote the manuscript. A.Y.N. suggested the model and supervised the development of the theory. J.M.-S., J.T.-G. and P.A.-G. carried out the simulations. Y.J., S.S., Y.Z. and K.K.-Z. contributed to the material synthesis. S.V., C.T., Z.D. and Y.Z. contributed to sample fabrication.

Competing interests R.H. is cofounder of Neaspec GmbH, a company producing scattering-type near-field scanning optical microscope systems, such as the one used in this study. The remaining authors declare no competing financial interests.

Additional information

Supplementary information is available for this paper at https://doi.org/10.1038/s41586-018-0618-9.

Reprints and permissions information is available at http://www.nature.com/reprints.

Correspondence and requests for materials should be addressed to P.A. or R.H. or Q.B.

Publisher's note: Springer Nature remains neutral with regard to jurisdictional claims in published maps and institutional affiliations.

METHODS

s-SNOM and nano-FTIR set-up. For infrared nano-imaging we used a scattering-type scanning near-field optical microscope (s-SNOM[3–5], from Neaspec). Metallized, cantilevered atomic force microscope (AFM) tips are used as scattering near-field probes. The tip is oscillating vertically at the mechanical resonant frequency (around 270 kHz) of the cantilever, with an amplitude of about 50 nm. The tip is illuminated with p-polarized infrared light of frequency ω (from tunable CO_2 and quantum cascade lasers) and electric E_{inc}, while the α-MoO_3 flake is raster-scanned below the oscillating tip. Acting as an infrared antenna, the Pt-coated tip concentrates the incident field into a nanoscale spot at the apex, which interacts with the sample surface and thus modifies the tip-scattered field E_{sca}. E_{sca} is recorded with a pseudo-heterodyne Michelson interferometer[34]. Demodulation of the interferometric detector signal at the nth harmonics of the tip oscillation frequency yields the complex-valued near-field signals $\sigma_n = s_n e^{i\varphi_n}$, with s_n being the near-field amplitude and φ_n being the near-field phase. By recording the near-field signals as a function of the lateral tip position, we obtain near-field images or line trace. In the particular case of probing a material supporting polaritons, the nanoscale 'hotspot' at the tip apex acts as a local source of polaritons[3–5]. The tip-launched polaritons reflect at the flake edges and produce polariton interference, yielding fringes in the near-field images (Figs. 2b, 3a, b). The distance between the interference fringes corresponds to half the polariton wavelength, $\lambda/2$.

For nano-FTIR spectroscopy[35], the tip was illuminated by a broadband super-continuum laser, and the tip-scattered light was recorded with an asymmetric Fourier transform spectrometer. By recording point spectra as a function of the tip position, we obtained high-resolution spectral line scans[5].

Disk fabrication. Bulk MoO_3 crystals were grown via chemical vapour deposition. Commercial MoO_3 powder (Sigma-Aldrich) was evaporated in a horizontal tube furnace at 785 °C and was re-deposited as α-MoO_3 crystals at 560 °C. The deposition process was carried out in an inert environment (Ar flow of 200 sccm) at 1 torr[28]. The as-grown bulk crystals were then mechanically exfoliated and transferred onto a Si/SiO_2 (thickness 300 nm) substrate. The transferred flakes were inspected with an optical microscope and characterized via AFM, allowing the selection of large and homogeneous pieces with the desired thickness. The selected flake was then shaped into a disk by using focused Ga-ion beam milling in a FEI Helios 600 Nanolab dual beam system. In order to protect the surface of the disk from the implantation of Ga ions, the flake was first covered by placing a thin diamond shield (approximate dimensions $100\,\mu m \times 80\,\mu m \times 0.5\,\mu m$) on top of the flake using the tip of an Omniprobe micromanipulator. Using the ion beam, we then milled through both the diamond shield and the flake using a ring-shaped milling pattern, until we reached the substrate. The remaining parts of the diamond shield were then lifted off the surface using the Omniprobe micromanipulator to give only the disk-shaped flake separated from the bulk flake by a ring-shaped channel.

Conductivity model for MoO_3 layers. Modelling the α-MoO_3 flake as a 2D conductivity layer of zero thickness avoids the calculation of the fields inside the slab[22], and has been proven valid for in-plane isotropic 2D materials (for example, graphene[36] and transition layer polaritons[37]) with a layer thickness that is much smaller than the polariton wavelength $(d \ll \lambda)$. In the model, the effective conductivity for the isotropic layer is given by $\sigma_{\text{eff}} = [cd/(2i\lambda_0)]\varepsilon$, where ε is the in-plane isotropic permittivity (both ε and σ_{eff} are scalars). Note that σ_{eff} scales linearly with d, thus taking into account the effect of the small slab thickness. Analogously, we model the α-MoO_3 layer by an anisotropic in-plane conducting layer with zero thickness and an effective 2D conductivity tensor, $\hat{\sigma}_{\text{eff}}$. The generalized relation between the tensor $\hat{\sigma}_{\text{eff}}$ and the (2×2) permittivity tensor $\hat{\varepsilon} = \text{diag}(\varepsilon_{xx}, \varepsilon_{yy})$ is then given by $\hat{\sigma}_{\text{eff}} = (cd/2i\lambda_0)\hat{\varepsilon}$. Note that the model is independent of the out-of-plane permittivity component ε_{zz}, which subsequently does not enter into equation (1).

Data availability

All the data are available in the online version of the paper. The data that support the findings of this study are available from the corresponding authors on reasonable request.

34. Ocelic, N., Huber, A. & Hillenbrand, R. Pseudoheterodyne detection for background-free near-field spectroscopy. *Appl. Phys. Lett.* **89**, 101124 (2006).
35. Huth, F., Schnell, M., Wittborn, J., Ocelic, N. & Hillenbrand, R. Infrared-spectroscopic nanoimaging with a thermal source. *Nat. Mater.* **10**, 352–356 (2011).
36. Nikitin, A. Y. in *World Scientific Handbook of Metamaterials and Plasmonics* 307–338 (World Scientific Series in Nanoscience and Nanotechnology, World Scientific, Singapore, 2017).
37. Tilley, D. R. *Surface Polaritons: Electromagnetic Waves at Surfaces and Interfaces* (North-Holland Publishing Co., Amsterdam, 1982).